ADVANCED OPTICAL MATERIALS
www.advopticalmat.de

Co-Catalyst Free Efficient Photocatalytic CO_2 Reduction Using Facet-Engineered Polyhedral $CsPbBr_3$ Perovskite Nanocrystals

Subarna Biswas, Rajashree P. Mishra, Jit Satra, Ram Sewak, Jyotisman Rath, Anirban Mondal, Yatendra S. Chaudhary, and Nimai Mishra**

In the quest for efficient photocatalysts, cancrystal shape engineering outperform size reduction in enhancing photocatalytic performance? This is investigated using $CsPbBr_3$ perovskite nanocrystals (PNC) by comparing conventional amine-capped, 6-facet cubic morphology with newly developed 26-facet polyhedral nanocrystals synthesized via an amine-free approach. Surprisingly, the larger polyhedral PNCs are far better at converting CO_2 into CO, despite their lower surface-to-volume ratio than the 6-facet cubic PNCs. They achieve a total CO yield of 394 µmol g^{-1} with a conversion rate of 35.81 µmol g^{-1} h^{-1} without any help from extra co-catalysts. To the best of the author's knowledge, this represents the highest reported CO evolution rate using 3-dimensional PNCs as the sole photocatalyst, with performance comparable to or exceeding systems employing co-catalysts. This enhanced activity arises from longer excited-state lifetimes, improved charge transport, larger electrochemical surface area (ECSA), and a higher density of charge carriers, as confirmed by optical and electrochemical studies. Computational studies show that some specific facets of this polyhedra bind CO_2 molecules more strongly and provide the optimized binding energy to efficiently release the final product(CO). With excellent 12-h stability, these shape-controlled nanocrystals enable a pathway toward sustainable energy technology applications worldwide.

1. Introduction

Since the shift to an industrial, carbon-dependent economy, increasing CO_2 emissions have emerged as a critical environmental concern because of their role in driving climate change. While reducing emissions is the most direct solution, it may not always be feasible, especially in sectors where fossil fuels remain indispensable. An alternative strategy involves actively capturing and transforming CO_2 into valuable materials.[1, 2] Unsurprisingly, CO_2 conversion has attracted substantial research interest in recent years. CO_2 is a highly stable molecule, largely due to the strong carbon-oxygen bond energy (750 kJ mol^{-1}), which demands extreme temperatures and pressures for thermocatalytic processes.[3] However, other promising methods, such as utilizing light (photocatalysis)[4–6] or electrical energy (electrocatalysis),[7–9] offer viable pathways for conversion. Among these two catalytic processes, photocatalysis offers certain advantages over electrocatalysis.[10] Photocatalysis harnesses sunlight as a clean and renewable energy source, eliminating the need for external electrical bias and reducing operational costs.[11] Unlike electrocatalysis, it avoids electrode corrosion and mass transport limitations, making it ideal for large-scale applications(such as H_2 production, etc.) where continuous and cost-effective output is crucial. To date, the majority of photocatalytic studies have explored binary and ternary metal oxides (such as TiO_2, $SrTiO_3$, $BiVO_4$, metal sulfides, etc.)[12–19] and chalcogen-based semiconductors (such as CdS, CdSe, etc.).[20–25] However, these conventional photocatalysts have several inherent limitations, such as insufficient light-harvesting capability due to wide band gaps (e.g., metal oxides)[26, 27] or sluggish charge transport due to trap states (e.g., CdS, CdSe, etc.).[28–30]

S. Biswas, J. Rath, N. Mishra
Department of Chemistry
Institute of Chemical Technology Mumbai
Indian Oil Odisha Campus Bhubaneswar
IIT Kharagpur Extension Center
Samantipuri Mouza
Gajapati Nagar, Bhubaneswar, Odisha 751013, India
E-mail: n.mishra@iocb.ictmumbai.edu.in

The ORCID identification number(s) for the author(s) of this article can be found under https://doi.org/10.1002/adom.202503043

DOI: 10.1002/adom.202503043

R. P. Mishra, Y. S. Chaudhary
Materials Chemistry Department
CSIR-Institute of Minerals and Materials Technology
Bhubaneswar 751013, India
E-mail: yschaudhary@immt.res.in

J. Satra
Energy and Environmental Laboratory
Institute of Physics
Bhubaneswar, Odisha 751005, India

R. Sewak, A. Mondal
Department of Chemistry
Indian Institute of Technology Gandhinagar
Palaj, Gujarat 382355, India

In light of these limitations, researchers are actively exploring operationally stable semiconductor photocatalysts with broader optical absorption and better charge transport properties to achieve superior photocatalytic performance. Given these requirements, perovskite nanocrystals with both of these features can be a potential option for photocatalysis.[31, 32] In fact, recent advances have showcased metal halide perovskite nanocrystals (PNCs) with the formula ABX_3 (where A is Cs^+, B is Pb^{2+}, and X^- is a halide in our case), emerging as one of the most versatile semiconductor materials.[33–36] Their versatility stems from superior absorption coefficients, tunable band gaps, exceptional defect tolerance, and long carrier diffusion lengths.[37–42]

Notably, these outstanding properties combine with the feasibility of low-cost, solution-processed synthesis at mild temperatures (≈140–180 °C).[37, 43] These exceptional features have already enabled breakthroughs in perovskite-based solar cells,[35, 44, 45] light-emitting diodes,[46–51] photodetectors,[52–54] and X-ray imaging,[55, 56] and now their potential in photocatalysis is being actively explored.[6, 57, 58] In addition to these superior properties, the context of photocatalytic CO_2 reduction reaction (CO_2RR), $CsPbX_3$ nanocrystals exhibit exceptional promise with conduction band minima (from 1.0 to −0.5 eV vs NHE) ideally positioned to drive thermodynamically favorable CO_2 photoreduction pathways.[59]

These functional properties of PNCs engendered considerable promise that halide perovskites may open up new avenues for photocatalytic CO_2 reduction. However, reports that successfully showcase both good photocatalytic activity and long-term operational stability in this domain are still less. These suboptimal performances of PNCs mainly stem from their weak ionic bonds and low lattice energy, leading to their degradation in polar solvents.[60, 61] Moreover, in nonpolar environments, light-induced degradation also results in the structural breakdown of PNCs.[62, 63] Another obstacle for facile charge transport arises from the presence of long-chain nonconducting ligands, which are used to synthesize the PNCs.[64–66] In addition, the small number of active sites on the PNC surface also leads to low conversion efficiency of CO_2 molecules.[67]

A successful strategy to overcome these challenges must simultaneously pursue at least three objectives: 1) enhancing material stability, 2) facilitating efficient charge separation, and 3) maximizing the ECSA and density of active facets. The material stability can be enhanced by surface modification with ligands, doping, or encapsulation, among other methods.[61, 68–71] Yet the issues of deactivation of carriers by exciton recombination, as well as a small number of active sites, persist. To enhance performance, co-catalysts like noble metals, metal oxides, metal–organic frameworks (MOF), and/or 2D materials (like rGO, Mxenes, etc.) are often integrated with PNCs.[72–80] They rapidly extract photogenerated charge carriers to prolong their separation, provide active sites to boost CO_2 reduction efficiency, and may often improve operational stability.

However, the in situ growth of PNCs within a cocatalyst framework (like MOF, etc.) is often challenging, and various degrees of optimization are still required for metal and metal oxide cocatalysts, such as controlling their size, exposed facets, and surface structure to suppress competing side reactions such as hydrogen evolution.[23, 81–85] The fine-tuning of these cocatalyst parameters poses a significant hurdle for standard techniques like Hot Injection and ligand-assisted reprecipitation synthesis (LARP).[86]

In this regard, polyhedral nanocrystals with their extra active facets and expanded surface area render them a good potential candidate to reduce the reliance on additional co-catalysts. In addition, PNCs with these unusual morphologies can impact the charge dynamics favorably for efficient photoredox activity through inherent properties like slower hot carrier cooling or suppression of the Auger process, etc.[87–89] Despite these advantages, their application in photocatalysis remains scarcely explored, with only a single study by Pradhan et al. addressing this potential to the best of our knowledge.[67] Therefore, it is evident that there is considerable scope for improving their synthesis strategy for functionality and catalytic performance.

In this work, we have systematically targeted facet-dependent photocatalytic CO_2 reduction using newly designed 26-faceted polyhedral $CsPbBr_3$, achieved through a single-step method that completely eliminates long-chain amines. Through comparative study against conventional 6-faceted $CsPbBr_3$ PNCs, we report that polyehedral PNCs show better photoredox activity toward CO_2 reduction, achieving a CO conversion yield of 394 μmole gm^{-1} without using any additional co-catalysts. The resulting CO_2 conversion efficiency not only exceeds all reported 3D PNC-based systems that operate without co-catalysts but also is comparable to or even superior to the majority of reported PNC systems that rely on co-catalysts. This amine-free sample also shows strong structural robustness during CO_2 photoreduction, maintaining operational stability for 12 h. We attribute the superior performance of these multifaceted PNCs over cubic PNCs to four synergistic factors, confirmed by detailed optical, electrochemical, and computational studies. These include i) ≈1.6 times higher excited-state lifetime, ii) nearly 1.7 times lower charge transport resistance due to short chain trioctylphopshine (TOP) ligands, iii) ≈1000 times higher excited-state carrier concentration with favorable flat band potential, and iv) an almost three-times greater ECSA (quantified by CO stripping voltammetry), which enhances performance by promoting facile CO_2 adsorption and feasible CO desorption on the different active facets of the amine-free $CsPbBr_3$ polyhedra. The optimized design of this polyhedral $CsPbBr_3$ PNC puts forth a new field of nanocrystals as a proficient photocatalyst for CO_2 conversion, creating opportunities for novel paths in renewable energy transformation.

2. Results and Discussion

In the amine-free synthesis, the higher effective growth solution concentration, together with a TOP/oleic acid–dominated ligand environment and longer growth time, results in growth kinetics that differ markedly from those in amine-containing conditions. These kinetic differences are directly reflected in the morphological evolution of the nanocrystals, ultimately leading to a pronounced divergence in nanocrystal shape.

We have previously established that[90] TOP is mostly oxidized in situ to trioctylphosphine oxide (TOPO), which plays a key role in shape control through steric-driven, site-selective surface passivation. These considerations collectively point to a growth mechanism governed by steric accessibility and facet-dependent ligand binding. The possible mechanism could be owing to its moderately large cone angle arising from three long

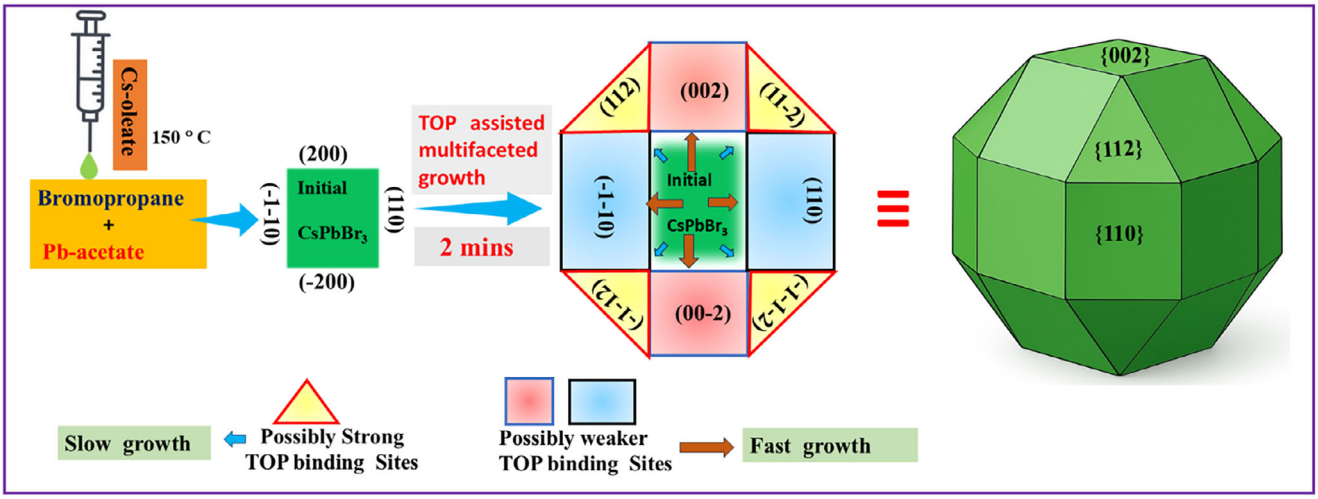

Scheme 1. The proposed growth mechanism of polyhedral $CsPbBr_3$ PNCs. Cs-oleate injection at 160 °C to produce cubic-shaped $CsPbBr_3$ PNCs in an orthorhombic phase (2D view). Then TOP/TOPO aided facet-dependent ligand binding leads to produce polyhedral morphology with various triangular (e.g., 112) and square-like facets[(200) and (110)] grown by facet-dependent ligand binding.

alkyl chains; TOP/TOPO cannot uniformly access all crystallographic surfaces. Instead, it preferentially binds to sterically accessible Pb-rich sites (most likely the high-index facets, where under-coordinated atoms are more prevalent) that provide a favorable coordination geometry, resulting in intrinsically nonuniform surface coverage. The strong Lewis base character of the P≐O moiety enables TOPO to effectively saturate exposed Pb sites on these accessible facets, substantially reducing their surface reactivity. Consequently, growth along TOPO-passivated directions is suppressed, while fewer ligand surfaces (lower index facets with fewer undercoordinated sites) remain weakly passivated and continue to grow rapidly, producing pronounced multifaceted growth. Thus, competition between strongly and weakly passivated surfaces drives the morphological evolution from cubic to complex polyhedral nanocrystals. It is noteworthy that, beyond these kinetic effects, ligand-poor facets undergo thermodynamic stabilization through surface reconstruction and geometric rearrangements that minimize total surface energy. This allows the crystal to adopt a balanced polyhedral morphology in which ligand-protected and unprotected facets coexist.

In contrast, OAm, owing to its linear structure, can access most surface Pb sites and distribute uniformly. This uniform passivation equalizes growth rates along different crystallographic directions, maintaining isotropic growth and resulting in cubic nanocrystals. Our proposed TOP-assisted growth mechanism for polyhedral CsPbBr3 PNC is presented in **Scheme 1**.

Despite the different growth mechanisms, both variants show apparently similar absorbance and emission spectra. However, the amine-free PNC exhibits a narrower emission peak (lower FWHM ≈ 17 nm compared to 23 nm for amine PNC) and slightly red-shifted first excitonic absorbance peak as well as emission peak compared to the amine-PNC, as depicted in **Figure 1**A,B. The PLQY of amine- and TOP-capped $CsPbBr_3$ PNCs is comparable, with a slight reduction for TOP-capped samples. This slight decrease arises because TOP selectively stabilizes facets where it binds but leaves few defects on inaccessible surfaces, and these mostly dormant type traps marginally reduce radiative recombination. In toluene medium, the amine-free PNC exhibits a longer excited-state lifetime than its amine-containing counterpart (Figure 1C), indicating a greater degree of electronic delocalization. Time-resolved PL decays of both samples were fitted using tri-exponential functions (see Table S1 and Section S3, Supporting Information), resolving fast (τ_1), intermediate (τ_2), and long-lived decay components(τ_3). Notably, the amine-free PNC shows an increased relative contribution from the long-lived component, which leads to a higher fraction of delocalized charge carriers in polyhedral $CsPbBr_3$ PNCs.

To check the effect of the CO_2 reaction medium on excited-state decay kinetics, TCSPC experiments in ethyl acetate-methanol medium (60:1 volume ratio) have also been performed. The amine-free PNC exhibits almost no change in excited state lifetime, whereas there is almost a 2.4 ns decrease in lifetime of for amine-capped PNCs.

This behavior arises from the polar nature of ethyl acetate, which accelerates ligand detachment from amine-capped PNCs and promotes trap-state formation. In contrast, the stronger binding of TOP in amine-free PNCs suppresses ligand-loss-assisted trap formation, rendering the excited-state decay kinetics largely insensitive to solvent polarity. This response is consistent with the polyhedral surface, in which strongly bound ligands stabilise selected facets, while the remaining ligand-poor facets achieve stability through intrinsic structural relaxation that lowers the overall surface energy, thereby preserving excited-state dynamics even in a polar medium.

Powder X-ray diffraction (XRD) patterns of amine- and amine-free $CsPbBr_3$ PNCs (Figure 1D) confirm the orthorhombic phase in all samples. For clarity, the terms “6-faceted” and “26-faceted” describe the external morphology of the nanocrystals rather than their crystal phase and reflect the shape evolution arising from ligand-controlled growth. Although TOP induces a polyhedral morphology through selective surface passivation, the bulk lattice of the nanocrystals remains orthorhombic, which is probed by XRD. The XRD patterns of both samples closely match the reference structure reported in the Crystallography Open Database

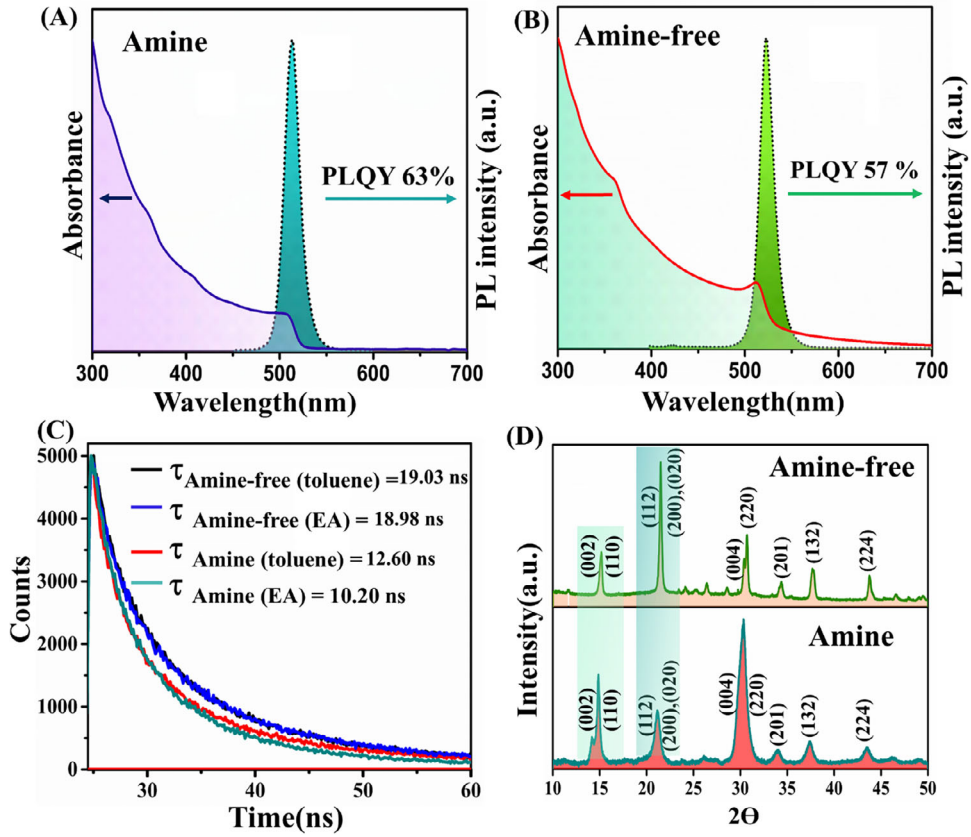

Figure 1. A) Absorption and PL spectra of amine-PNC measured in Toluene. B) Absorption and PL spectra of amine-free PNCs measured in Toluene. C) lifetime of both the samples in toluene and ethyl acetate-methanol medium. D) XRD patterns of amine-PNC and amine-free PNCs.

(COD: 1 533 062), confirming phase purity and structural consistency across the two systems. Interestingly, the (110) and (002) reflections near 15° show visible splitting in the amine-capped PNCs, indicating greater $[PbBr_6]^{4-}$ octahedral distortion and symmetry lowering. In contrast, the weaker splitting observed for the polyhedral amine-free PNCs suggests a relatively less distorted and more structurally stabilized Pb–Br framework. This trend may be associated with facet-selective binding of bulky TOP/TOPO ligands, which preferentially passivate sterically accessible facets and can locally restrict octahedral tilting at the surface, thereby limiting the extent of symmetry lowering within the Pb–Br framework. As a result, the amine-free PNCs display smaller peak splitting near 15° in the XRD patterns compared to their amine-capped counterparts. In addition, the XRD intensity near ≈21° is sharply enhanced in amine-free PNCs compared to amine-capped samples. In this region, the high-index (112) reflection lies in close proximity to the low-index (200) and (020) reflections due to their comparable interplanar spacings. In amine-capped PNCs, isotropic growth leads to the simultaneous contribution of multiple crystallographic planes, resulting in a broadened diffraction feature rather than a well-defined peak. By contrast, the intense and sharp peak observed for amine-free PNCs indicates that a single set of planes dominates the diffraction response. If both high- and low-index reflections were enhanced to a similar extent, partial peak overlap or significant broadening would be expected, reflecting a nonselective growth process similar to that of the amine-capped PNCs. Such behavior is inconsistent with the formation of well-defined polyhedral morphologies.

At this stage, based on the proposed growth model, we anticipate that the high-index (112) facet is slow-growing, whereas one of the low-index facets, (200) or (020), grows more rapidly. This selective growth behavior is consistent with the dominance of a sharp diffraction feature near ≈21°, while the real-space manifestation of the slow-growing (112) facet is later supported by HRTEM analysis.

Structurally, amine-capped PNCs show cubic morphology (≈11 ±2 nm) (**Figure** 2A), while TOP-capped PNCs form 26-faceted rhombicuboctahedra (≈24 ± 2 nm) (Figure 2B), which in two-dimensional TEM projections appear as truncated octahedron outlines with multiple intersecting edges arising from the simultaneous exposure of low- and high-index facets.

The size distribution of both is represented in Figure S1 (Supporting Information). HRTEM of cubic-shaped amine-capped PNC (inset of Figure 2A) confirms a lattice spacing of 0.59 nm corresponding to (110) planes of orthorhombic $CsPbBr_3$ phase, while a lattice spacing of 0.41 nm in amine-free PNC corresponds to the (200) facet (inset of Figure 2B).

Further insight into the polyhedral morphology is obtained from Fast Fourier Transform (FFT) analysis of the HRTEM images represented in Figure 2C, which reveals multiple distinct lattice spacings within a single 2D octagonal projection, confirming the simultaneous exposure of different crystallographic planes.

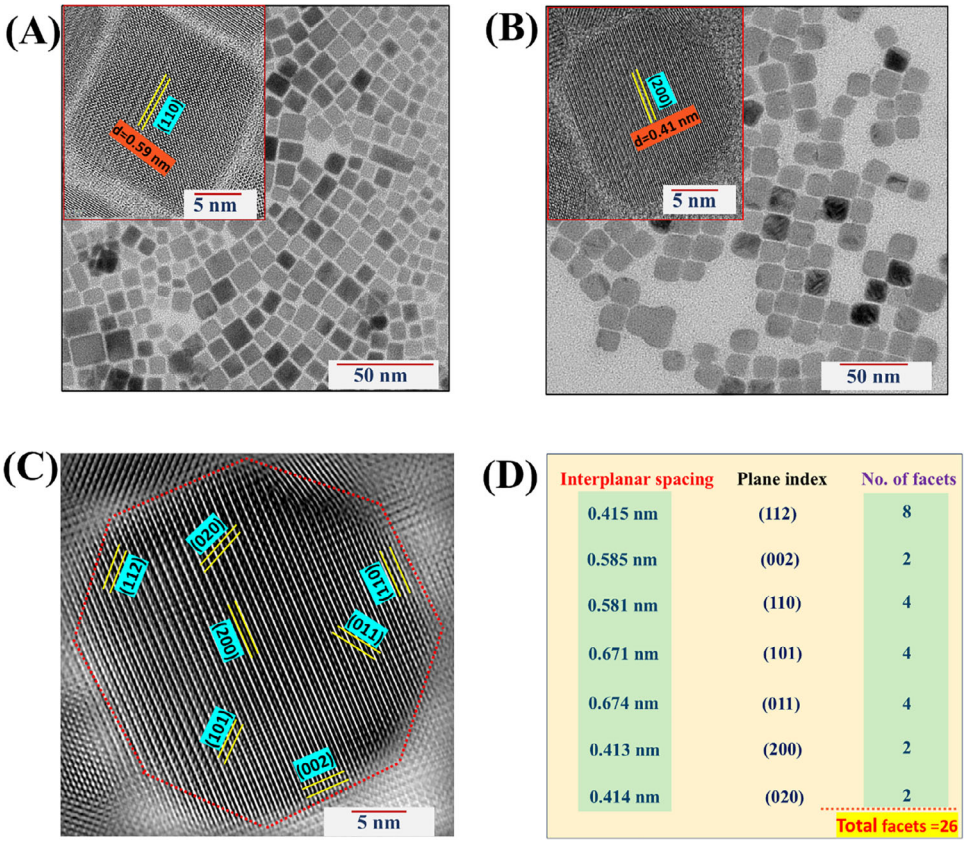

Figure 2. A) TEM and HRTEM image(inset) of amine-capped $CsPbBr_3$. B) TEM and HRTEM image(inset) of amine-free polyhedral $CsPbBr_3$. C) FFT analysis of the HRTEM image of amine-free $CsPbBr_3$. D) Different (*h*, *k*, *l*) values and their combinations to reflect amine-free 26 faceted $CsPbBr_3$ nanocrystals.

Indexing of the FFT spots shows that the polyhedral morphology comprises distinct facet types, including triangular (112) facets, square (110) facets, rectangular (002) facets, etc. On this basis, we construct a facet-indexing chart in Figure 2D, that outlines the possible plane combinations contributing to the formation of the 26-faceted rhombicuboctahedral morphology. This analysis provides direct structural evidence that the complex 26 facet polyhedral shape originates from the concurrent stabilization of multiple facet families induced by ligand-controlled growth by TOP.

To understand the inherent charge transport properties for photocatalysis, the as-prepared nanocrystals were subjected to different photoelectrochemical (PEC) characterizations. To investigate their intrinsic properties crucial for photocatalytic activity, such as the charge transfer efficiency, probable band energy diagram, and photosensitivity, electrochemical impedance spectra (EIS), Mott–Schottky analysis, and chronoamperometric techniques were employed. EIS reveals distinct differences in charge-transfer resistance (R_{ct}) between amine-free and amine-capped PNCs (**Figure** 3A). Analysis using the conventional Randles circuit model (see Figure S2, Supporting Information) yields R_{ct} values of 1550 Ω for amine-free PNCs and 2500 Ω for amine-capped PNCs. The significantly lower R_{ct} of the amine-free PNCs highlights their superior charge-transfer capability compared to their amine-containing counterparts. This enhanced performance arises because TOP binds selectively rather than uniformly, leaving portions of the polyhedral surface relatively less ligand-dense. These partially exposed facets do not introduce additional resistance to charge transport. Moreover, where TOP is present, its short-chain nature imposes a reduced tunnelling barrier, further facilitating facile charge transfer across the interface. In contrast, the long-chain OAm ligands in amine-capped PNCs impose a larger charge transport barrier, thereby hindering electron transfer. Overall, both surface stabilization and ligand density play critical roles in governing the charge-transport efficiency of PNC catalysts.

To investigate the probable band positions for evaluating the capable redox activity of targeted photocatalysis and associated excited-state charge carrier densities of the catalysts, Mott–Schottky analysis was performed using capacitance-voltage measurements at a frequency of 100 Hz (Figure 3B) under 100 mW cm^{-2} light illumination. The Mott–Schottky plot exhibits a fitted straight line that has a positive slope, indicating the n-type semiconducting nature of the catalyst. Its intersection on the x-axis gives the flat-band potential, which is a measure of the probable position for the conduction band. The more negative value of flat-band potential for amine-free PNC suggests a lower space charge transport barrier in terms of reduction potential of CO_2, validating its higher catalytic activity with respect to amine PNCs. The relative position of the flat band potential of amine and amine-free PNCs with respect to the CO_2 to CO redox potential is represented in Figure 3C. From the slope, the

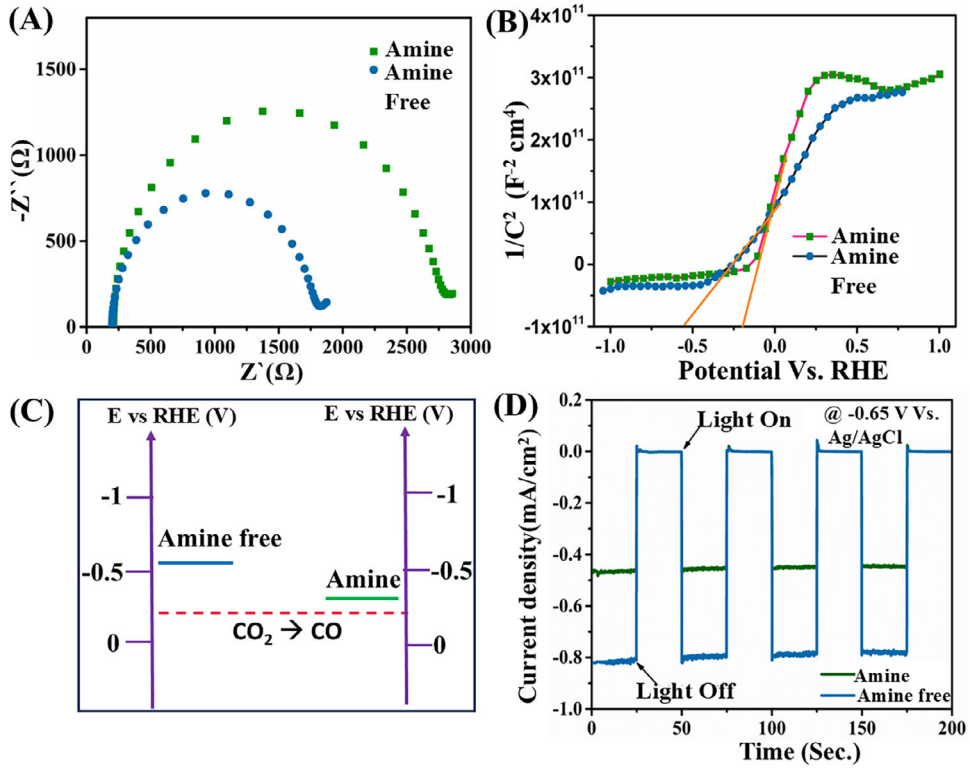

Figure 3. A) Impedance spectra (Nyquist plot) recorded at −0.65 V Ag/AgCl under continuous illumination. B) Mott–Schottky plot of amine-PNC and amine-free PNC. C) Band energy diagram representing the position of flat band potential for both amine and amine-free PNCs. D) Amperometric *I–t* curve measured at −0.65 VAg/AgCl under 100 mW cm^{-2} under light on-off conditions.

associated excited state carrier concentration was determined, and it is observed that there is a significant enhancement in carrier concentration in amine-free PNCs (**Table 1**) as compared to amine-PNCs, which is an indication of higher catalytic property. In addition to charge-transfer resistance analysis, ECSA estimated from EIS provides complementary insight. While not directly correlated with photocatalytic activity, the ECSA serves as an indicator of the accessible catalytic surface. The amine-free PNCs exhibit a higher ECSA than their amine-capped counterparts, consistent with their lower charge-transfer resistance. This suggests that the removal of bulky OAm ligands exposes more active sites, thereby enhancing the effective surface area available for catalysis.

Figure 3D represents current versus time plots of the prepared nanostructures measured at −0.65 V versus Ag/AgCl under chopped light illumination. It is evident from these results that both the catalysts are significantly photo-sensitive. But the higher ratio of I_{light} /I_{dark} (See Table 1) for amine-free PNCs with respect to amine-capped is a direct reflection of lower R_{ct}. All these electrochemical characterizations provide critical insight into the charge-transfer kinetics, probable band energetics, photosensitivity, and accessible catalytic surface area of photocatalysts. In light of these combined advantages, amine-free PNCs emerge as a more favorable platform for efficient photocatalytic CO_2 reduction.

The photocatalytic CO_2 reduction performance of these nanocrystals was evaluated in the ethyl acetate and methanol mixture system (60:1 volume ratio). The reason for taking ethyl acetate was to balance polarity and high CO_2 solubility, and methanol was chosen not only for quenching photogenerated holes but also as a source of protons (H^+). **Figure** 4A shows the GC analysis used to evaluate the amount of products (CO) formed during CO_2 photoreduction. This is further confirmed by a prominent signal at m/z value of 28 (shown in Figure S3, Supporting Information), which indicates CO is the primary reduced product upon light irradiation. The near-linear increase in CO concentration over time, coupled with the absence of other products, confirms the high selectivity for CO during CO_2 reduction.

Table 1. Parameters obtained from electrochemical characterizations.

Material	Charge transfer resistance [Ω]	Flat band potential [V]	Carrier concentration [per cm^3]	I_{light}/I_{dark}	C_{dl} [F]	ECSA [cm^2]
Amine $CsPbBr_3$	2500	−0.21	1.25×10^{17}	282	3.5×10^{-6}	70
Amine-free $CsPbBr_3$	1550	−0.55	2.70×10^{20}	507	10×10^{-6}	200

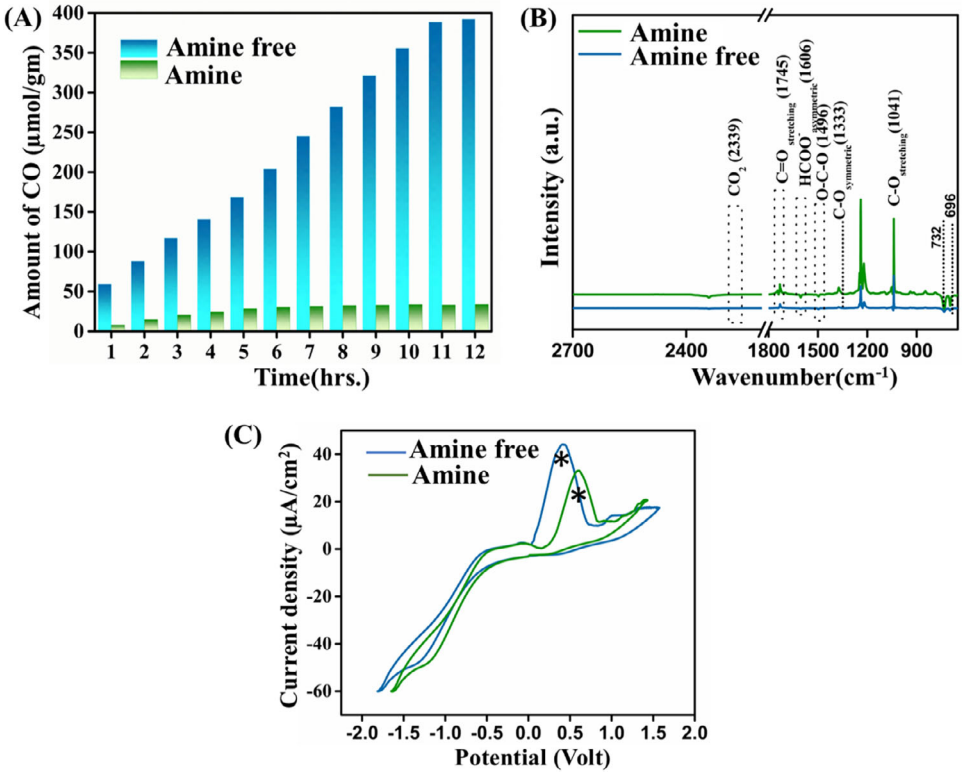

Figure 4. A) Histograms showing the formation of CO from CO_2 reduction reactions after 6 h using amine and amine-free $CsPbBr_3$ nanostructures as photocatalysts. B) FTIR spectra of the reaction mixture after 12 h of photocatalytic reactions with amine and amine-free PNCs. C) CO stripping voltammetry profiles of amine and amine-free $CsPbBr_3$ PNCs.

Among the tested catalysts, amine-capped cubic $CsPbBr_3$ PNCs yield only 34 µmol g^{-1} of CO, whereas amine-free polyhedral nanocrystals exhibit a pronounced enhancement in activity, delivering a maximum CO yield of 394 µmol g^{-1} with an evolution rate of 35.81 µmol g^{-1} h^{-1}. To ensure that the observed CO originates from CO_2 reduction, blank control experiments were conducted to quantify CO contributions from the photo-reformation of the ethyl acetate-methanol solvent mixture (60:1) in the presence of both catalysts. The solvent-derived CO was negligible relative to CO_2-saturated conditions (see Figure S4, Supporting Information) and was therefore subtracted from the total CO yield. The corrected CO evolution rates are presented in Figure 4A. A comparison with previously reported perovskite-based photocatalysts is provided in Table S2 (Section S3, Supporting Information), where the present system outperforms most PNCs, even those integrated with co-catalysts. Time-resolved product evolution further reveals that the amine-free polyhedral PNCs sustain nearly linear CO generation for up to 11 h, followed by a gradual slowdown, while the amine-capped cubic PNCs show an early decline in activity after only ≈6 h. This performance disparity is possibly linked to site-selective TOP attachments across crystallographic facets of polyhedral amine-free PNCs. Facets that develop in the absence of proximal TOP remain ligand-poor and expose clean surface sites, enabling efficient adsorption of small and linear CO_2 molecules. Moreover, even TOP-coordinated facets can also permit CO_2 access through inter-ligand spacing. In contrast, the densely packed OAm layer sterically restricts CO_2 adsorption. Moreover, in TOP-capped polyhedral PNCs, both ligand-stabilized and relatively ligand-poor facets remain structurally robust in polar media, consistent with the facet-selective stabilization mechanism discussed earlier. OAm-capped nanocrystals, however, undergo ligand loss in polar environments, leading to trap-state formation and suppressed charge transport. The superior CO_2 reduction activity of amine-free PNCs therefore emerges from the coupled effects of enhanced surface accessibility, preserved electronic structure, efficient charge transport, and optimized CO_2 adsorption and CO desorption energetics (discussed later). Consistent with this surface-driven superiority, the electrochemical and optical measurements discussed before also provide direct insight into the origin of the enhanced activity of amine-free polyhedral $CsPbBr_3$. These results reveal that, together with a favorable polyhedral surface architecture, a synergistic combination of prolonged excited-state lifetime, reduced charge-transport resistance, increased electroactive surface area, higher excited-state carrier concentration, and optimized CO_2 adsorption collectively drives the superior photocatalytic performance.

To gain deeper insight into the reaction intermediates formed during the CO_2RR, attenuated total reflectance Fourier-transform infrared (ATR-FTIR) spectroscopy was employed. In Figure 4B, the peak observed at 2339 cm^{-1} is associated with the asymmetric stretching vibrations of CO_2, while the peaks at 1333, 1496, 1606, and 1745 cm^{-1} correspond to the C—O symmetric stretching in COOH, an antisymmetric O—C—O stretch band, asymmetric stretching vibration of $HCOO^-$, and C═O stretching of surface-bound CO intermediate, respectively. The peak at 1041

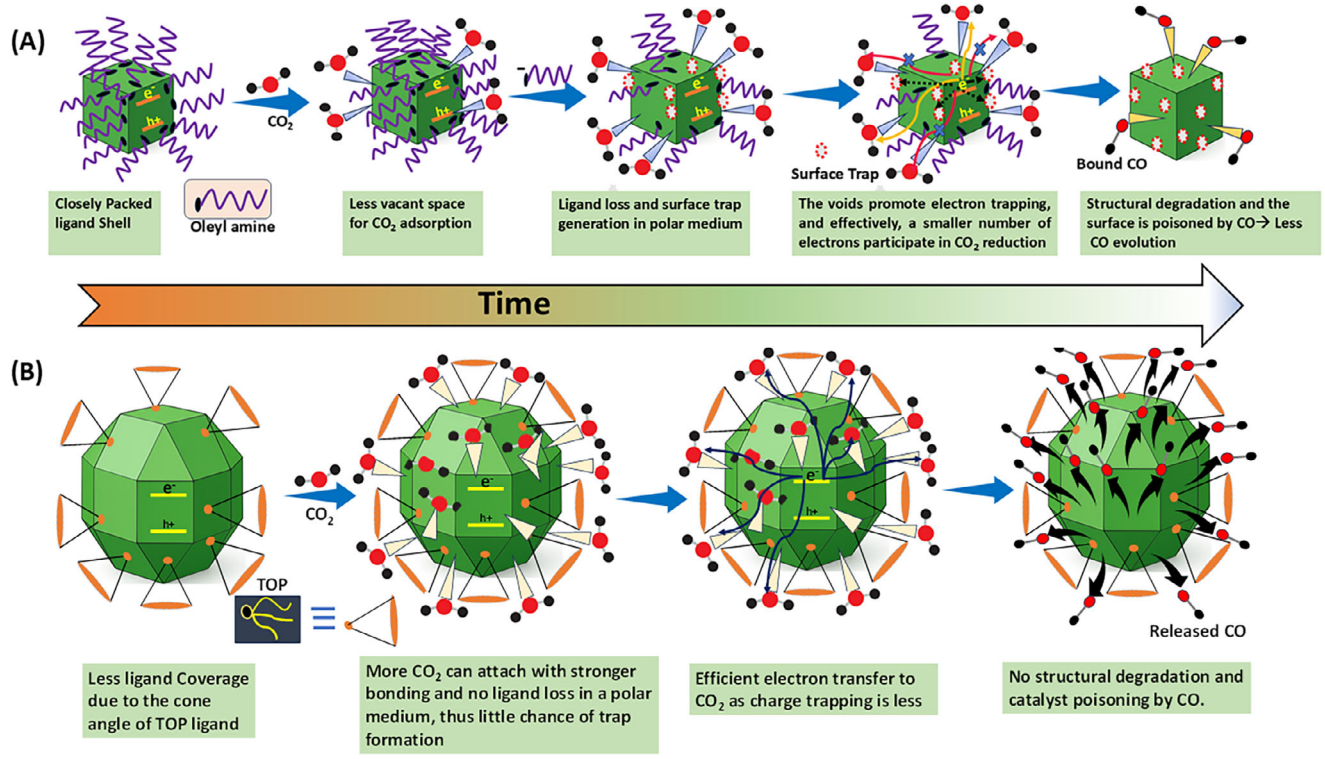

Scheme 2. A schematic illustration highlighting the role of nonuniform surface interactions, ligand-driven stability, CO_2 and/or CO adsorption dynamics, and degradation pathways.

cm^{-1} is attributed to the C—O stretching mode of HCO_3^- (bicarbonate) or CO_3^{2-} (carbonate) species, indicating CO_2 adsorption and surface stabilization. In the low wavelength region, the peaks at 696 and 732 cm^{-1} observed during the CO_2 reduction to CO are related to the symmetric deformation of the CO_3^{2-} species and bending vibrations of surface-bound HCO_3^- (bicarbonate) or CO_3^{2-} (carbonate) species. These vibrational features collectively confirm the stepwise activation and transformation of CO_2 on the catalyst surface, highlighting the formation of key intermediates such as $COOH^-$, $HCOO^-$, bicarbonate, and surface-bound CO, revealing the underlying reaction pathway of CO_2 reduction to CO.[91]

To probe product formation kinetics, we further performed electrochemical CO stripping voltammetry in post-catalytic solutions to get an idea about the CO binding strength on both PNC surfaces, as evident from Figure 4C. The stripping curve of both amine and amine-free PNCs consisted of two major distinct peaks located before PNC's oxidation peak (marked by *), corresponding to the oxidation of adsorbed CO at different facets of PNCs. The CO stripping peaks of amine-free PNCs show three pronounced features compared to those of amine-based PNCs: i) relatively high peak intensity, ii) more peak broadening, and iii) lower CO oxidation potential. The high CO oxidation peak intensity denotes a higher active surface area, which indicates a greater amount of CO coverage. This can also be correlated to the higher ECSA value obtained for amine-free PNCs before (Table 1). The relatively broader nature of the CO oxidation peak indicates involvement of different types of facets in comparison to amine-based PNCs. The lower CO oxidation potential suggests weaker CO adsorption on the amine-free PNCs surface. Therefore, all aforementioned factors, i.e., higher catalytic surface area and involvement of multiple facets with coverage with weak CO binding, facilitate the CO_2 photo reduction toward CO formation in amine-free PNCs compared to their amine-based analogues.

A schematic illustration of the above-mentioned phenomena, highlighting the role of nonuniform interactions, ligand-driven stability, CO_2 and CO adsorption dynamics, and degradation pathways, is presented in **Scheme 2**, which captures how these combined factors ultimately lead to superior CO_2 conversion in amine-free polyhedral PNCs.

To investigate the structural and chemical evolution following 12-h prolonged catalytic operation, post-catalytic optical and structural analysis of the amine-free $CsPbBr_3$ nanocrystals was conducted. From **Figure 5**A,B, it is evident that the optical absorbance spectra and crystal phase remained largely unchanged even after 12 h of catalytic testing, and it is consistent with the sustained CO_2 reduction activity observed over 12 h. However, the post-catalytic absorption spectra exhibit an absorption tail extending beyond the first excitonic peak, indicative of the generation of surface defect states or scattering caused by nanocrystal aggregation and surface inhomogeneity during prolonged photocatalysis. In parallel, the XRD patterns show slightly broadened or split diffraction peaks(e.g., ≈31°), suggesting a minor distortion of the PNC octahedral domains during extended photocatalysis. Nevertheless, these changes remain marginal and do not signify any substantial structural alteration. Consistent with this observation, TEM images in Figure 5C show that the polyhedral morphology remains intact after catalysis, while HRTEM

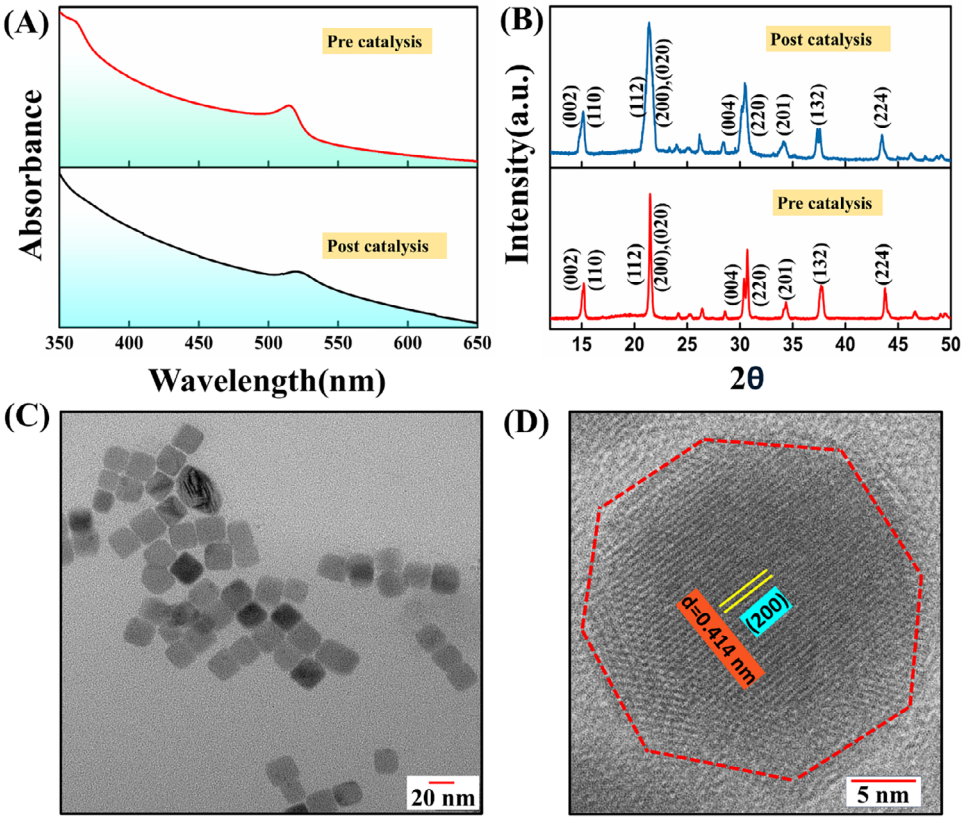

Figure 5. A) Comparison of the absorbance spectra before and after the catalysis (12 h) for an amine-free $CsPbBr_3$ sample. B) XRD pattern of amine-free $CsPbBr_3$ before and after catalysis. C) TEM image of amine-free $CsPbBr_3$ after catalysis. D) HRTEM image of amine-free $CsPbBr_3$ after 12 h of catalysis.

in Figure 5D reveals well-resolved lattice fringes with interplanar spacings identical to those prior to catalysis.

Further, to get insight into the CO_2 reduction mechanism, DFT-based electronic structure calculations were performed. Effective CO_2 reduction requires strong chemisorption of CO_2 on $CsPbBr_3$ facets, prompting the selection of surfaces with high CO_2 adsorption energy. Conversely, optimal product (CO in our case) production requires intermediate binding for facile desorption from active sites. The binding energy optimization is also essential for any efficient catalytic process. An excessively high binding energy of CO_2 relative to CO may lead to catalyst poisoning. In this state, active sites of PNCs are occupied and blocked by strongly adsorbed CO_2, preventing further catalytic cycles. Consequently, a large kinetic barrier is introduced, stalling the reaction at the initial stage and resulting in a diminished product yield. Conversely, if CO binds too strongly relative to CO_2, the product desorption rate is severely limited. This slow release of the desired product similarly poisons the active sites and results in a diminished overall yield.

For our calculations, a slab model of the CsBr-terminated (001) surface of orthorhombic $CsPbBr_3$ was chosen, as it has been previously identified as the most stable surface configuration and is capped with a single OAm molecule.[92] In contrast, to simulate amine-free PNC, we evaluated CO_2 and CO adsorption on all relevant surface planes, i.e., (100), (110), and (111) of $CsPbBr_3$ passivated with a single TOP molecule. These surfaces, particularly with CsBr terminations, have been theoretically studied in previous work for their stability and were selected accordingly. The adsorption energies of CO_2 and CO molecules on both amine-capped and amine-free $CsPbBr_3$ surfaces are summarized in Table 1. It can be seen that the amine-free PNC exhibits greater CO_2 adsorption energies on the (100) and (111) planes compared to the amine-capped samples. Notably, for the amine-free (110) surface, the adsorption energies are positive for both molecules, indicating endothermic and thermodynamically unfavorable adsorption processes as summarised in **Table 2**.

The highest adsorption energy is observed for the amine-free (100)-CsBr surface, followed by (111) surface. This can be attributed to the greater structural relaxation and higher ionicity of the surface layer, which have been previously reported to enhance surface stability.

Furthermore, based on the experimental observation of enhanced CO_2 reduction activity on TOP-capped $CsPbBr_3$, our DFT calculations suggest that amine-free nanocrystals with improved CO_2 adsorption capacity predominantly expose due to a higher proportion of (100) and (111) facets in their polyhedral morphology. This result is consistent with CO stripping voltammetry data, which indicates that the amine-free catalyst facilitates CO_2 reduction across multiple crystal facets. Moreover, the relative binding energy values of CO_2 with respect to CO (i.e, CO_2 binding energy/CO binding energy for different facets) for amine-free samples are lower than it's amine-based counterparts. This optimized environment reduces the likelihood of catalyst poisoning and directly explains the superior product yield of amine-free $CsPbBr_3$

Table 2. Adsorption energy (eV) for CO_2 or CO molecules on various surfaces.

Adsorption energy	Amine-capped	Amine-free (100)	Amine-free (110)	Amine-free (111)
CO_2	−0.703	−0.874	2.357	−0.864
CO	−0.069	−0.204	4.434	−0.186

over the amine-based catalyst. The optimized top-view configurations of the adsorbed molecules on various surfaces are shown in Figure S5 (Supporting Information). It can be observed that, in all cases, the oxygen atoms preferentially interact with the Cs atoms.

The charge density difference analysis has also been performed to further investigate charge redistribution upon the adsorption of CO_2 and CO molecules, as shown in **Figure 6**. Charge density difference plots for CO_2 adsorption on amine-capped (001), amine-free PNCs (100) and (111) facets are represented in Figure 6A,B,C, respectively. While CO adsorption on the same facet of amine-capped and amine-free PNCs is shown in 6(D), 6(E), and 6(F), respectively. In both cases, charge accumulation occurs near the adsorbed molecules, while charge depletion appears at Cs atom on the slab surface.

However, the interaction of CO_2 and CO molecules with the surface involves charge transfer between the terminal oxygen atoms and surface Cs atoms. In the case of CO_2, this interaction induces a long-range polarization effect due to the symmetric linear structure of the molecule, leading to significant charge accumulation on one of the terminal oxygen atoms. In contrast, the CO molecule, which has an intrinsically asymmetric charge distribution, undergoes only short-range polarization, resulting in less charge accumulation on the terminus O and weaker adsorption. As a consequence, CO_2 binds more strongly to both amine-capped and amine-free perovskite surfaces (specifically the (100) and (111) facets) compared to the CO molecule. This stronger binding is advantageous for the desired catalytic conversion under investigation, as mentioned before.

To establish a mechanistic connection between surface chemistry and catalytic performance, we therefore evaluated the complete free-energy landscape of the CO_2 reduction reaction on representative amine-capped and amine-free $CsPbBr_3$ surfaces. This analysis clarifies how surface-dependent energetics govern CO_2 activation, intermediate stabilization, and CO release. The free-energy profiles for the CO_2 reduction pathway were analyzed on the amine-capped (100) and amine-free (111) surfaces to elucidate their distinct catalytic behaviors represented in **Figure 7**, while the detailed reaction free-energy values for each elementary step are summarized in Table S3 (Supporting Information). The first step, CO_2 adsorption (ΔG_1), is more favorable on the amine-free (111) surface (−1.88 eV) than on the amine-capped (100) surface (−0.73 eV), indicating stronger CO_2 binding on the (111) termination. This trend continues in the hydrogenation step to form the COOH intermediate: ΔG_2 is significantly more exergonic on the amine-free (111) surface compared to the

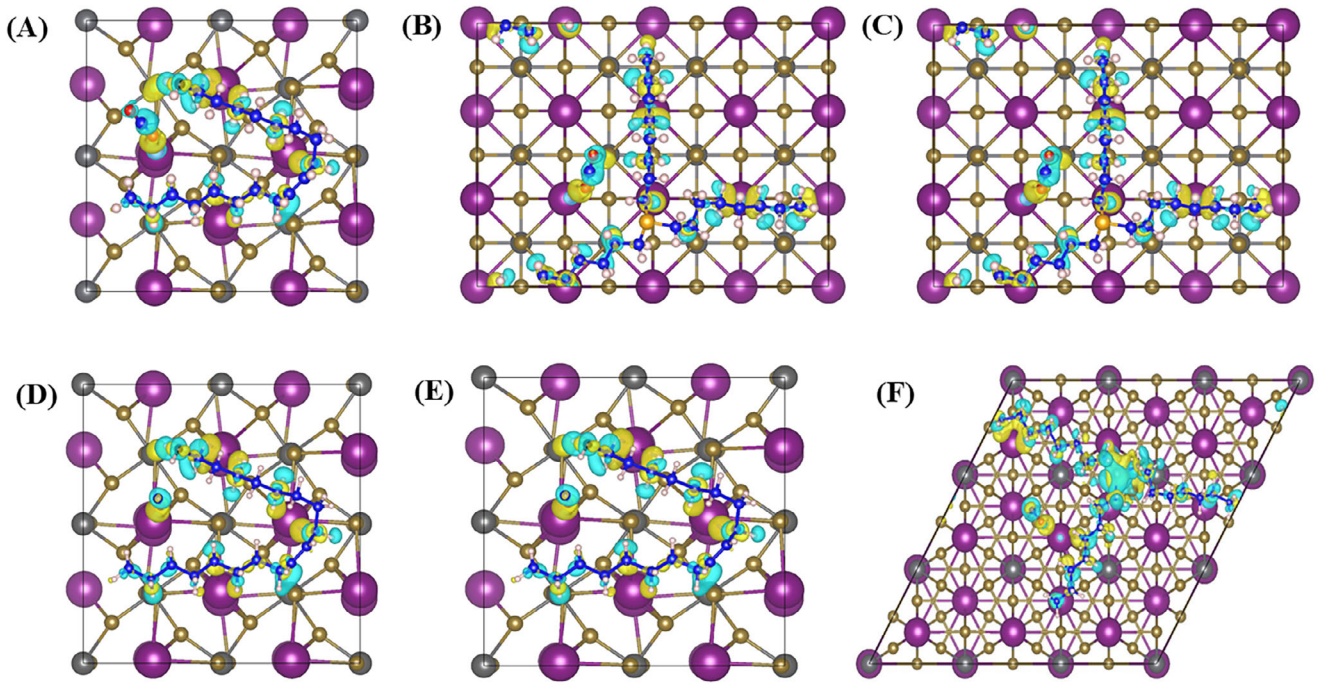

Figure 6. Charge density difference plot for A) CO_2 adsorbed amine-capped PNC. B) CO_2 adsorbed amine-free PNC(100) plane. C) CO_2 adsorbed amine-free PNC(111) plane. D) CO adsorbed amine-capped PNC, E) CO adsorbed amine-free PNC(100) plane, and F) CO adsorbed amine-free PNC(111) plane. Yellow and blue regions represent electron accumulation and depletion, respectively, with an isosurface value of 0.00052 e $Å^{-3}$.

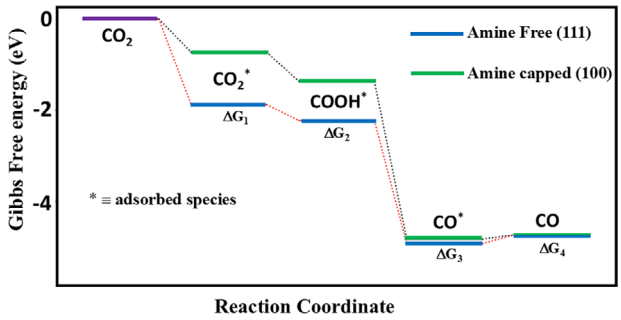

Figure 7. DFT-calculated Gibbs free energy profiles for CO_2 reduction to CO on amine and amine-free $CsPbBr_3$ PNC surfaces. The amine-free surface shows reduced free energy barriers, indicating more favorable reaction kinetics and consistent with the enhanced experimental CO_2 reduction activity.

amine-capped (100) surface, suggesting enhanced stabilization of the *COOH species on the (111) facet. The subsequent conversion of COOH to CO and H_2O (ΔG_3) is thermodynamically favorable on both surfaces; although both are strongly exergonic, the (111) surface again exhibits slightly more favorable energetics. Finally, the free energy for CO desorption (ΔG_4) is nearly identical for the two systems. The results show that the amine-free (111) surface exhibits more favorable energetics throughout the pathway compared to the amine-capped (100) surface, while the stronger adsorption on the (111) facet does not hinder CO desorption. Overall, the DFT analysis qualitatively rationalizes the experimentally observed enhanced CO_2 reduction kinetics of amine-free PNCs by revealing a thermodynamically more favorable reaction landscape with improved stabilization of CO_2-derived intermediates. This lowered energetic cost across key elementary steps supports faster charge utilization and sustained CO evolution, consistent with the superior catalytic performance observed experimentally.

3. Conclusion

In conclusion, the morphology-dependent photocatalytic activity of $CsPbBr_3$ nanostructures is explored, taking conventional amine-capped 6-faceted and our newly synthesized 26-faceted TOP-capped $CsPbBr_3$ PNCs. Surprisingly, larger polyhedral $CsPbBr_3$ PNCs exhibited superior catalytic performance over smaller cubic-shaped ones, indicating that the presence of highly active facets is a more important factor than surface area alone in these systems. Detailed optical and electrochemical studies confirm the enhanced performance of TOP-capped $CsPbBr_3$ PNCs over amine-capped ones. This enhancement stems from several key advantages of polyhedral PNCs, they are: i) easy surface accessibility of CO_2 molecules, ii) ≈1.6 times higher excited-state lifetime, iii) ≈1.7 times lower charge transport resistance, iv) ≈3 times greater electroactive surface area, v) ≈1000 times

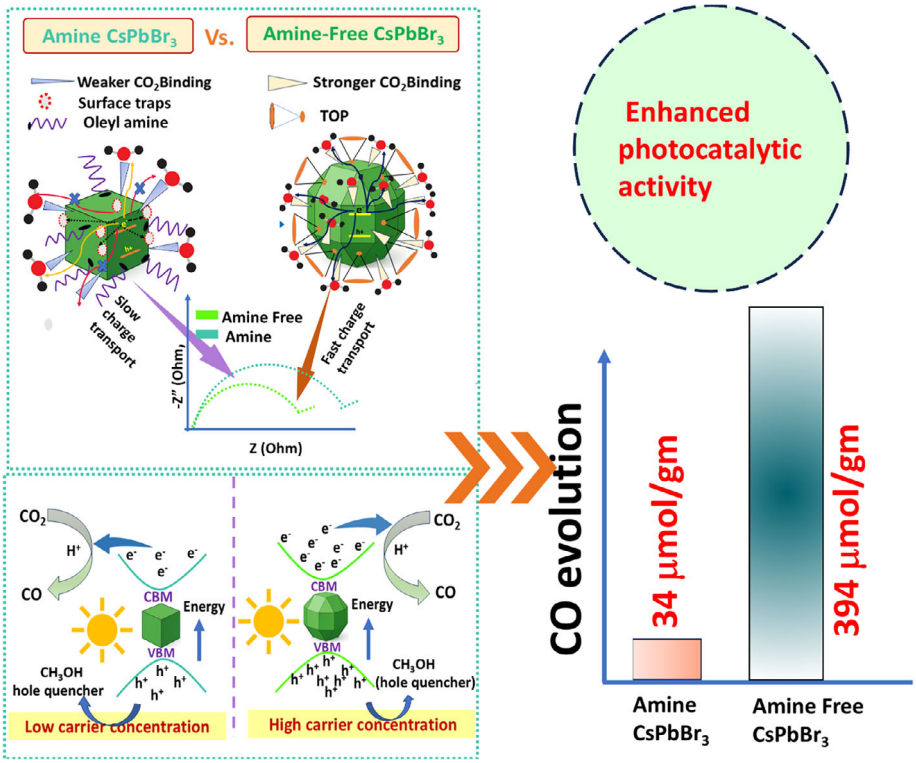

Scheme 3. Schematic illustration highlighting the key reason behind the greater photocatalytic activity of amine-free PNCs with respect to amine PNCs. CO_2 binds weakly on the amine-capped cubic surface, and partial ligand loss in the polar reaction medium leads to higher interfacial charge transport resistance, limiting interfacial charge delivery to adsorbed CO_2. In contrast, facet-selective TOP binding stabilizes polyhedral PNCs, enabling stronger CO_2 adsorption with minimal obstruction to charge transport. Concurrently, the polyhedral PNCs sustain a higher excited-state carrier population under illumination. The synergistic effects of enhanced CO_2 binding, efficient charge transport, and increased carrier availability collectively result in a substantially higher CO_2 conversion rate for TOP-capped polyhedral PNCs.

increased charge carrier concentration along with catalytically favorable band potential, and vi) robust operational stability. The fundamental origin of this performance is further elucidated by surface-specific studies. DFT calculations confirm stronger CO_2 adsorption on the polyhedral PNC surface, suggesting faster photoreduction kinetics. Complementing this, CO stripping voltammetry also reveals a higher density of active sites with optimal intermediate CO binding energy, which ensures efficient product desorption and completes the highly effective catalytic cycle. Collectively, these factors enable the amine-free system to not only surpass amine-capped $CsPbBr_3$ PNCs but also to achieve the highest reported CO yield (394 μmol g^{-1}) with an average rate of 35.81 μmol g^{-1} h^{-1} among all studies employing unsupported three-dimensional perovskite nanocrystals as the sole catalyst, to the best of our knowledge. Remarkably, its efficiency is either comparable or even exceeds that of systems integrating PNCs with other external co-catalysts as well. The amine-free $CsPbBr_3$ PNCs also maintain excellent stability over an extended period (12 h), making them a highly stable photocatalyst. The key reason behind the greater photocatalytic activity of amine-free PNCs is schematically represented in **Scheme 3**. Thus, we can envision that our polyhedral perovskite nanocrystals could unlock a new platform for advanced photocatalysis, opening avenues for sustainable environmental applications and energy-efficient technologies.

4. Experimental Section

Material Synthesis: Both the 26-faceted polyhedral and 6-faceted $CsPbBr_3$ nanocrystals were synthesized by adopting our previously reported methods (synthetic details are mentioned in Supporting Information).[93] In short, the three-precursor approach has been adopted for the synthesis of polyhedral $CsPbBr_3$ PNCs, where 1-bromopropane and lead acetate were used as a Br and Pb precursor, respectively. Unlike oleyl amine, the most commonly used ligand for PNC synthesis, trioctylphosphine (TOP) was used as a capping ligand for polyhedral $CsPbBr_3$ synthesis. The Cs-oleate solution was injected at 160 °C, and the reaction was allowed to proceed for 2 min before being quenched in an ice bath.

Amine-capped $CsPbBr_3$ (PNCs) were synthesized following the conventional hot injection method. Briefly, $PbBr_2$ was dissolved in octadecene (ODE) with oleylamine (OAm) and oleic acid (OA) and heated to 160 °C under stirring. Caesium oleate was then swiftly injected, and the reaction was quenched after 5 s by immersion in an ice bath to yield amine-$CsPbBr_3$ PNCs. The product was isolated by centrifugation and washed before further use. Detailed synthesis procedures are mentioned in Supporting Information.

Electrochemical Measurement: To perform electrochemical measurements, the PNC samples were coated on a poly-methyl methacrylate (PMMA) and reduced graphene oxide (rGO) modified ITO substrate (exposed surface area: 0.25 cm^2) in a similar way to the previous work.[68] This PNC-coated ITO substrate acts as a working electrode. The whole experiment was run in a 0.1 (M) solution of tetrabutylammonium hexafluorophosphate ($TBAPF_6$) in ethyl acetate and methanol medium under 100 mW cm^{-2} solar irradiation in a three-electrode cell where Ag/AgCl was taken as a reference and a Pt-wire as a counter electrode.

Photocaralytic CO_2 Reduction: Visible-light-driven photocatalytic CO_2 reduction was performed in a sealed reaction vessel under simulated solar irradiation (300 W Xe lamp, 1 sun illumination, >420 nm cut-off filter). The photocatalyst (10 mg) was dispersed in 15 mL of ethyl acetate containing 250 μL methanol. Prior to irradiation, the reactor was purged with Ar and subsequently with high-purity CO_2 for 60 min to remove air and saturate the system. After CO_2 saturation, illumination was initiated to conduct the photocatalytic reaction at 25 °C. Gaseous products were analyzed using a gas chromatograph (GC) with a TCD detector, and product identities were confirmed by GC-MS. See Supporting Information (Experimental Details) for details.

Supporting Information

Supporting Information is available from the Wiley Online Library or from the author.

Acknowledgements

The authors sincerely acknowledge the Institute of Chemical Technology Mumbai—Indian Oil Odisha Campus, Bhubaneswar, and the CSIR-Institute of Minerals and Materials Technology (IMMT), Bhubaneswar, for providing instrumental facilities and support. The authors are grateful to Dr. Nirmal Goswami (CSIR-IMMT) for support with various experimental facilities. The authors are thankful to Mrinalkanti Panda from NISER, Bhubaneswar, for TRPL measurements. RS and AM thank PARAM Ananta for computational resources. This research was also supported by the Core Research Grant (CRG/2022/005380) from DST-SERB.

Conflict of Interest

The authors declare no conflict of interest.

Author Contributions

S.B. and R.P.M. contributed equally to this work. N.M. and Y.S.C. conceptualized the study and provided overall supervision. J.S. and J.R. performed the electrochemical analysis along with S.B. DFT calculations and analyses were carried out by R.S. and A.M. S.B. wrote the initial draft, and then all authors contributed to the manuscript based on their respective areas of expertise.

Data Availability Statement

The data that support the findings of this study are available on request from the corresponding author. The data are not publicly available due to privacy or ethical restrictions.

Keywords

amine free, CO_2 reduction, co-catalyst free, multifacet, photocatalysis

Received: September 15, 2025
Revised: January 4, 2026
Published online:

[1] A. Goeppert, M. Czaun, J.-P. Jones, G. K. Surya Prakash, G. A. Olah, *Chem. Soc. Rev.* **2014**, *43*, 7995, https://doi.org/10.1039/C4CS00122B.
[2] X.-H. Liu, J.-G. Ma, Z. Niu, G.-M. Yang, P. Cheng, *Angew. Chem., Int. Ed.* **2015**, *54*, 988, https://doi.org/10.1002/anie.201409103.
[3] S. Xie, Q. Zhang, G. Liu, Y. Wang, *Chem. Commun.* **2016**, *52*, 35, https://doi.org/10.1039/C5CC07613G.
[4] J. Rath, S. Sukanya, S. Biswas, N. Mishra, *Cryst. Growth Des.* **2024**, *24*, 6549, https://doi.org/10.1021/acs.cgd.4c00409.

[5] S. R. Lingampalli, M. M. Ayyub, C. N. R. Rao, *ACS Omega* **2017**, *2*, 2740.
[6] S. Fang, M. Rahaman, J. Bharti, E. Reisner, M. Robert, G. A. Ozin, Y. H. Hu, *Nat. Rev. Methods Primers* **2023**, *3*, 61, https://doi.org/10.1038/s43586-023-00243-w.
[7] S. Nitopi, E. Bertheussen, S. B. Scott, X. Liu, A. K. Engstfeld, S. Horch, B. Seger, I. E. L. Stephens, K. Chan, C. Hahn, J. K. Nørskov, T. F. Jaramillo, I. Chorkendorff, *Chem. Rev.* **2019**, *119*, 7610, https://doi.org/10.1021/acs.chemrev.8b00705.
[8] D. Bagchi, S. Roy, S. Ch Sarma, S. C. Peter, *Adv. Funct. Mater.* **2022**, *32*, 2209023, https://doi.org/10.1002/adfm.202209023.
[9] S. Mondal, S. C. Peter, *Adv. Mater.* **2024**, *36*, 2407124, https://doi.org/10.1002/adma.202407124.
[10] A. Chakravorty, S. Roy, *Sustain. Chem. Environ.* **2024**, *8*, 100155, https://doi.org/10.1016/j.scenv.2024.100155.
[11] X. She, Y. Wang, H. Xu, S. Chi Edman Tsang, S. Ping Lau, *Angew. Chem., Int. Ed.* **2022**, *61*, 202211396, https://doi.org/10.1002/anie.202211396.
[12] S. N. Habisreutinger, L. Schmidt-Mende, J. K. Stolarczyk, *Angew. Chem., Int. Ed.* **2013**, *52*, 7372, https://doi.org/10.1002/anie.201207199.
[13] A. L. Linsebigler, G. Lu, J. T. Yates, *Chem. Rev.* **1995**, *95*, 735, https://doi.org/10.1021/cr00035a013.
[14] C. Avcıoğlu, S. Avcıoğlu, M. F. Bekheet, A. Gurlo, *ACS Appl. Energy Mater.* **2023**, *6*, 1134.
[15] Y. Zhang, X. Wu, Z.-H. Wang, Y. Peng, Y. Liu, S. Yang, C. Sun, X. Xu, X. Zhang, J. Kang, S.-H. Wei, P. F. Liu, S. Dai, H. G. Yang, *J. Am. Chem. Soc.* **2024**, *146*, 6618, https://doi.org/10.1021/jacs.3c12062.
[16] S. Heckel, M. Wittmann, M. Reid, K. Villa, J. Simmchen, *Acc. Mater. Res.* **2024**, *5*, 400, https://doi.org/10.1021/accountsmr.3c00021.
[17] S. Wang, C. Li, Y. Qi, J. Zhang, N. Wang, M. Liu, B. Zhang, X. Cai, H. Zhang, S. Wei, G. Ma, J. Yang, S. Chen, F. Zhang, *Nat. Commun.* **2025**, *16*, 3776, https://doi.org/10.1038/s41467-025-59076-8.
[18] R. P. Mishra, M. Mrinalini, N. Kumar, S. Bastia, Y. S. Chaudhary, *Langmuir* **2023**, *39*, 14189, https://doi.org/10.1021/acs.langmuir.3c01064.
[19] N. Kumar, R. P. Mishra, B. Dash, S. Bastia, Y. S. Chaudhary, *J. Mater. Chem. A* **2023**, *11*, 20839, https://doi.org/10.1039/D3TA03267A.
[20] Y. Jiang, E. A. Weiss, *J. Am. Chem. Soc.* **2020**, *142*, 15219, https://doi.org/10.1021/jacs.0c07421.
[21] S. Lee, Y. Lee, H. G. Abbas, S. Ji, S. Y. Kim, K. Lee, S. Li, E. J. Lee, J. Choi, H. Ahn, I. Y. Kim, S.-I. In, S. Ringe, Y. J. Jang, J. Yang, *Nano Lett.* **2025**, *25*, 7351, https://doi.org/10.1021/acs.nanolett.5c00529.
[22] R. Bera, A. Dutta, S. Kundu, V. Polshettiwar, A. Patra, *J. Phys. Chem. C* **2018**, *122*, 12158, https://doi.org/10.1021/acs.jpcc.8b02108.
[23] A. Agosti, Y. Nakibli, L. Amirav, G. Bergamini, *Nano Energy* **2020**, *70*, 104510, https://doi.org/10.1016/j.nanoen.2020.104510.
[24] F. Qiu, Z. Han, J. J. Peterson, M. Y. Odoi, K. L. Sowers, T. D. Krauss, *Nano Lett.* **2016**, *16*, 5347, https://doi.org/10.1021/acs.nanolett.6b01087.
[25] H. Li, C. Cheng, Z. Yang, J. Wei, *Nat. Commun.* **2022**, *13*, 6466, https://doi.org/10.1038/s41467-022-34263-z.
[26] N. Serpone, A. V. Emeline, *J. Phys. Chem. Lett.* **2012**, *3*, 673, https://doi.org/10.1021/jz300071j.
[27] W. Jiang, H. Loh, B. Q. L. Low, H. Zhu, J. Low, J. Z. X. Heng, K. Y. Tang, Z. Li, X. J. Loh, E. Ye, Y. Xiong, *Appl. Catal., B* **2023**, *321*, 122079, https://doi.org/10.1016/j.apcatb.2022.122079.
[28] T. Goldzak, A. R. McIsaac, T. Van Voorhis, *Nat. Commun.* **2021**, *12*, 890, https://doi.org/10.1038/s41467-021-21153-z.
[29] C. Pu, X. Peng, *J. Am. Chem. Soc.* **2016**, *138*, 8134, https://doi.org/10.1021/jacs.6b02909.
[30] F. P. García de Arquer, D. V. Talapin, V. I. Klimov, Y. Arakawa, M. Bayer, E. H. Sargent, *Science 373*, aaz8541, https://doi.org/10.1126/science.aaz8541.
[31] J. T. DuBose, P. V. Kamat, *ACS Energy Lett.* **2022**, *7*, 1994.
[32] A. Dey, J. Ye, A. De, E. Debroye, S. K. Ha, E. Bladt, A. S. Kshirsagar, Z. Wang, J. Yin, Y. Wang, L. N. Quan, F. Yan, M. Gao, X. Li, J. Shamsi, T. Debnath, M. Cao, M. A. Scheel, S. Kumar, J. A. Steele, M. Gerhard, L. Chouhan, K. Xu, X.-G. Wu, Y. Li, Y. Zhang, A. Dutta, C. Han, I. Vincon, A. L. Rogach, et al., *ACS Nano* **2021**, *15*, 10775, https://doi.org/10.1021/acsnano.0c08903.
[33] I. M. Asuo, D. Gedamu, N. Y. Doumon, I. Ka, A. Pignolet, S. G. Cloutier, R. Nechache, *Adv. Mater.* **2020**, *1*, 1866.
[34] Q. A. Akkerman, V. D'Innocenzo, S. Accornero, A. Scarpellini, A. Petrozza, M. Prato, L. Manna, *J. Am. Chem. Soc.* **2015**, *137*, 10276, https://doi.org/10.1021/jacs.5b05602.
[35] H. Min, D. Y. Lee, J. Kim, G. Kim, K. S. Lee, J. Kim, M. J. Paik, Y. K. Kim, K. S. Kim, M. G. Kim, T. J. Shin, S. Il Seok, *Nature* **2021**, *598*, 444, https://doi.org/10.1038/s41586-021-03964-8.
[36] P. Ding, D. Chen, P. K. Ko, M. Qammar, P. Geng, L. Guo, J. E. Halpert, *Nanoscale* **2025**, *17*, 1148, https://doi.org/10.1039/D4NR04012K.
[37] L. Protesescu, S. Yakunin, M. I. Bodnarchuk, F. Krieg, R. Caputo, C. H. Hendon, R. X. Yang, A. Walsh, M. V. Kovalenko, *Nano Lett.* **2015**, *15*, 3692, https://doi.org/10.1021/nl5048779.
[38] M. V. Kovalenko, L. Protesescu, M. I. Bodnarchuk, *Science* **2017**, *358*, 745, https://doi.org/10.1126/science.aam7093.
[39] A. Swarnkar, R. Chulliyil, V. K. Ravi, M. Irfanullah, A. Chowdhury, A. Nag, *Angew. Chem., Int. Ed.* **2015**, *54*, 15424, https://doi.org/10.1002/anie.201508276.
[40] H. Huang, M. I. Bodnarchuk, S. V. Kershaw, M. V. Kovalenko, A. L. Rogach, *ACS Energy Lett.* **2017**, *2*, 2071.
[41] G. W. P. Adhyaksa, L. W. Veldhuizen, Y. Kuang, S. Brittman, R. E. I. Schropp, E. C. Garnett, *Chem. Mater.* **2016**, *28*, 5259, https://doi.org/10.1021/acs.chemmater.6b00466.
[42] J. De Roo, M. Ibáñez, P. Geiregat, G. Nedelcu, W. Walravens, J. Maes, J. C. Martins, I. Van Driessche, M. V. Kovalenko, Z. Hens, *ACS Nano* **2016**, *10*, 2071, https://doi.org/10.1021/acsnano.5b06295.
[43] J. Shamsi, A. S. Urban, M. Imran, L. De Trizio, L. Manna, *Chem. Rev.* **2019**, *119*, 3296, https://doi.org/10.1021/acs.chemrev.8b00644.
[44] Q. A. Akkerman, M. Gandini, F. Di Stasio, P. Rastogi, F. Palazon, G. Bertoni, J. M. Ball, M. Prato, A. Petrozza, L. Manna, *Nat. Energy* **2016**, *2*, 16194, https://doi.org/10.1038/nenergy.2016.194.
[45] S. B. Shivarudraiah, N. Tewari, M. Ng, C.-H. A. Li, D. Chen, J. E. Halpert, *ACS Appl. Mater. Interfaces* **2021**, *13*, 37223, https://doi.org/10.1021/acsami.1c10657.
[46] P. K. Ko, J. Ge, P. Ding, D. Chen, H. L. T. Tsang, N. Kumar, J. E. Halpert, *Adv. Mater.* **2025**, *37*, 2407764, https://doi.org/10.1002/adma.202407764.
[47] B.-S. Zhu, Z.-Y. Ma, Y.-H. Song, J.-M. Hao, K.-H. Song, G.-J. Ding, Y.-L. Hu, Y.-P. Xie, Y.-C. Yin, H.-B. Yao, *Nano Lett.* **2024**, *24*, 14750, https://doi.org/10.1021/acs.nanolett.4c04121.
[48] D. Chen, P. K. Ko, C.-H. A. Li, B. Zou, P. Geng, L. Guo, J. E. Halpert, *ACS Energy Lett.* **2023**, *8*, 410, https://doi.org/10.1021/acsenergylett.2c02243.
[49] Y. Gao, Q. Cai, Y. He, D. Zhang, Q. Cao, M. Zhu, Z. Ma, B. Zhao, H. He, D. Di, Z. Ye, X. Dai, *Sci. Adv.* **2024**, *10*, ado5645, https://doi.org/10.1126/sciadv.ado5645.
[50] H. Wang, X. Zhang, Q. Wu, F. Cao, D. Yang, Y. Shang, Z. Ning, W. Zhang, W. Zheng, Y. Yan, S. V. Kershaw, L. Zhang, A. L. Rogach, X. Yang, *Nat. Commun.* **2019**, *10*, 665, https://doi.org/10.1038/s41467-019-08425-5.
[51] R. Wang, J. Zhao, J. Ma, C. Lu, Z. Yu, G. Tu, J. Zhang, *ACS Energy Lett.* **2024**, *9*, 4699, https://doi.org/10.1021/acsenergylett.4c01805.
[52] P. Ramasamy, D.-H. Lim, B. Kim, S.-H. Lee, M.-S. Lee, J.-S. Lee, *Chem. Commun.* **2016**, *52*, 2067, https://doi.org/10.1039/C5CC08643D.
[53] S. Wang, S. Yang, Z. Xu, H. Xu, G. Duan, D. Zhao, X. Wang, B. Cao, *J. Mater. Chem. C* **2025**, *13*, 902, https://doi.org/10.1039/D4TC03359K.

[54] Y. Li, Z.-F. Shi, S. Li, L.-Z. Lei, H.-F. Ji, D. Wu, T.-T. Xu, Y.-T. Tian, X.-J. Li, *J. Mater. Chem. C* **2017**, *5*, 8355, https://doi.org/10.1039/C7TC02137B.
[55] K. Sakhatskyi, B. Turedi, G. J. Matt, E. Wu, A. Sakhatska, V. Bartosh, M. N. Lintangpradipto, R. Naphade, I. Shorubalko, O. F. Mohammed, S. Yakunin, O. M. Bakr, M. V. Kovalenko, *Nat. Photonics* **2023**, *17*, 510, https://doi.org/10.1038/s41566-023-01207-y.
[56] Y. Liu, C. Gao, D. Li, X. Zhang, J. Zhu, M. Wu, W. Liu, T. Shi, X. He, J. Wang, H. Huang, Z. Sheng, D. Liang, X.-F. Yu, H. Zheng, X. Sun, Y. Ge, *Nat. Commun.* **2024**, *15*, 1588, https://doi.org/10.1038/s41467-024-45871-2.
[57] S. Mondal, S. Banerjee, S. Bera, S. Mondal, S. P. Midya, R. Jana, R. K. Behera, A. Datta, N. Pradhan, P. Ghosh, *ACS Catal.* **2024**, *14*, 6633, https://doi.org/10.1021/acscatal.4c01643.
[58] A. Mathuri, B. Pal, M. Pramanik, A. Manna, P. Mal, *Catal. Sci. Technol.* **2024**, *14*, 183, https://doi.org/10.1039/D3CY01478A.
[59] V. K. Ravi, G. B. Markad, A. Nag, *ACS Energy Lett.* **2016**, *1*, 665, https://doi.org/10.1021/acsenergylett.6b00337.
[60] S. Cheng, H. Zhong, *J. Phys. Chem. Lett.* **2022**, *13*, 2281, https://doi.org/10.1021/acs.jpclett.2c00166.
[61] S. Chatterjee, S. Biswas, S. Sourav, J. Rath, S. Akhil, N. Mishra, *J. Phys. Chem. Lett.* **2024**, *15*, 10118, https://doi.org/10.1021/acs.jpclett.4c02240.
[62] Z. Song, C. Wang, A. B. Phillips, C. R. Grice, D. Zhao, Y. Yu, C. Chen, C. Li, X. Yin, R. J. Ellingson, M. J. Heben, Y. Yan, *Sustainable Energy Fuels* **2018**, *2*, 2460, https://doi.org/10.1039/C8SE00358K.
[63] M. V. Khenkin, I. Visoly-Fisher, S. Kolusheva, Y. Galagan, F. Di Giacomo, O. Vukovic, B. R. Patil, G. Sherafatipour, V. Turkovic, H.-G. Rubahn, M. Madsen, A. V. Mazanik, E. A. Katz, *ACS Appl. Energy Mater.* **2018**, *1*, 799, https://doi.org/10.1021/acsaem.7b00256.
[64] N. Fiuza-Maneiro, K. Sun, I. López-Fernández, S. Gómez-Graña, P. Müller-Buschbaum, L. Polavarapu, *ACS Energy Lett.* **2023**, *8*, 1152, https://doi.org/10.1021/acsenergylett.2c02363.
[65] Q. Cao, J. Feng, K. T. Chang, W. Liang, H. Lu, *Adv. Mater.* **2025**, *37*, 2409096, https://doi.org/10.1002/adma.202409096.
[66] M.-G. Jeon, A. Kirakosyan, C. Shin, S. Yun, J. Kim, L. Li, J. Choi, *Chem. Eng. J.* **2023**, *462*, 142120, https://doi.org/10.1016/j.cej.2023.142120.
[67] S. Shyamal, S. K. Dutta, T. Das, S. Sen, S. Chakraborty, N. Pradhan, *J. Phys. Chem. Lett.* **2020**, *11*, 3608, https://doi.org/10.1021/acs.jpclett.0c01088.
[68] S. Biswas, M. K. Panda, S. Chatterjee, J. Satra, S. K. Sharma, J. Rath, A. Dutta, D. Acharjee, S. Chakraborty, S. Ghosh, N. Mishra, *Adv. Funct. Mater.* **2025**, *n/a*, 2505506, https://doi.org/10.1002/adfm.202505506.
[69] L. Li, L. Gan, Z. Zhang, *Adv. Mater. Interfaces* **2021**, *8*, 2100202, https://doi.org/10.1002/admi.202100202.
[70] S. Akhil, S. Biswas, M. Palabathuni, R. Singh, N. Mishra, *J. Phys. Chem. Lett.* **2022**, *13*, 9480, https://doi.org/10.1021/acs.jpclett.2c02403.
[71] S. Biswas, S. Akhil, N. Kumar, M. Palabathuni, R. Singh, V. G. V. Dutt, N. Mishra, *J. Phys. Chem. Lett.* **2023**, *14*, 1910, https://doi.org/10.1021/acs.jpclett.2c03772.
[72] T. Kawawaki, Y. Akinaga, D. Yazaki, H. Kameko, D. Hirayama, Y. Negishi, *Chem. – Eur. J.* **2023**, *29*, 202203387, https://doi.org/10.1002/chem.202203387.
[73] V. Phuaran, M. S. Ahmad, K. Sumi, P. R. Pratama, Y. Akaishi, M. Takafuji, P. Vas-Umnuay, T. Kida, *Nanoscale* **2025**.
[74] J. K George, A. Pasha, S. Mohan, R. G. Balakrishna, *ACS Appl. Nano Mater.* **2023**, *6*, 9464.
[75] Y.-F. Xu, M.-Z. Yang, B.-X. Chen, X.-D. Wang, H.-Y. Chen, D.-B. Kuang, C.-Y. Su, *J. Am. Chem. Soc.* **2017**, *139*, 5660, https://doi.org/10.1021/jacs.7b00489.
[76] A. Pan, X. Ma, S. Huang, Y. Wu, M. Jia, Y. Shi, Y. Liu, P. Wangyang, L. He, Y. Liu, *J. Phys. Chem. Lett.* **2019**, *10*, 6590, https://doi.org/10.1021/acs.jpclett.9b02605.
[77] Q.-M. Sun, J.-J. Xu, F.-F. Tao, W. Ye, C. Zhou, J.-H. He, J.-M. Lu, *Angew. Chem., Int. Ed.* **2022**, *61*, 202200872, https://doi.org/10.1002/anie.202200872.
[78] Y.-F. Mu, C. Zhang, M.-R. Zhang, W. Zhang, M. Zhang, T.-B. Lu, *ACS Appl. Mater. Interfaces* **2021**, *13*, 22314, https://doi.org/10.1021/acsami.1c01718.
[79] R. Tang, H. Sun, Z. Zhang, L. Liu, F. Meng, X. Zhang, W. Yang, Z. Li, Z. Zhao, R. Zheng, J. Huang, *Chem. Eng. J.* **2022**, *429*, 132137, https://doi.org/10.1016/j.cej.2021.132137.
[80] K. Lv, Z. Li, X. Huang, Z. Cheng, Z. Wang, H. Zhao, *Adv. Sci.* **2025**, *n/a*, 07747, https://doi.org/10.1002/advs.202507747.
[81] W.-N. Wang, W.-J. An, B. Ramalingam, S. Mukherjee, D. M. Niedzwiedzki, S. Gangopadhyay, P. Biswas, *J. Am. Chem. Soc.* **2012**, *134*, 11276, https://doi.org/10.1021/ja304075b.
[82] C. Dong, C. Lian, S. Hu, Z. Deng, J. Gong, M. Li, H. Liu, M. Xing, J. Zhang, *Nat. Commun.* **2018**, *9*, 1252, https://doi.org/10.1038/s41467-018-03666-2.
[83] P. Yang, L. Li, Z.-J. Zhao, J. Gong, *Chin. J. Catal.* **2021**, *42*, 817, https://doi.org/10.1016/S1872-2067(20)63692-0.
[84] X. Cai, A. Wang, J. Wang, R. Wang, S. Zhong, Y. Zhao, L. Wu, J. Chen, S. Bai, *J. Mater. Chem. A* **2018**, *6*, 17444, https://doi.org/10.1039/C8TA06204H.
[85] S. Bai, X. Wang, C. Hu, M. Xie, J. Jiang, Y. Xiong, *Chem. Commun.* **2014**, *50*, 6094, https://doi.org/10.1039/C4CC00745J.
[86] S. Akhil, S. Biswas, P. Manoj, N. Mishra, in *Perovskite Optoelectronic Devices*, (Ed.: B. Pradhan), Springer International Publishing, Cham **2024**, pp. 71–112.
[87] N. V. S. Praneeth, S. Akhil, A. Mukherjee, S. Seth, S. Khatua, N. Mishra, *Adv. Opt. Mater.* **2024**, *12*, 2303222, https://doi.org/10.1002/adom.202303222.
[88] D. Acharjee, A. Das, M. K. Panda, M. Barai, S. Ghosh, *Nano Lett.* **2023**, *23*, 1946, https://doi.org/10.1021/acs.nanolett.2c05107.
[89] K. J Babu, G. Kaur, A. Shukla, R. Saha, A. Kaur, M. Sachdeva, D. K. Yadav, H. N. Ghosh, *ACS Photonics* **2022**, *9*, 969, https://doi.org/10.1021/acsphotonics.1c01830.
[90] S. Akhil, V. G. V. Dutt, N. Mishra, *Nanoscale Adv.* **2021**, *3*, 2547, https://doi.org/10.1039/D1NA00091H.
[91] B. Innocent, D. Pasquier, F. Ropital, F. Hahn, J.-M. Léger, K. B. Kokoh, *Appl. Catal., B* **2010**, *94*, 219, https://doi.org/10.1016/j.apcatb.2009.10.027.
[92] Y. Yang, F. Gao, S. Gao, S.-H. Wei, *J. Mater. Chem. A* **2018**, *6*, 14949.
[93] S. Akhil, V. G. V. Dutt, N. Mishra, *Nanoscale* **2021**, *13*, 13142, https://doi.org/10.1039/D1NR03560F.